J. Fluid Mech. (2023), *vol*. 969, A6, doi:10.1017/jfm.2023.555

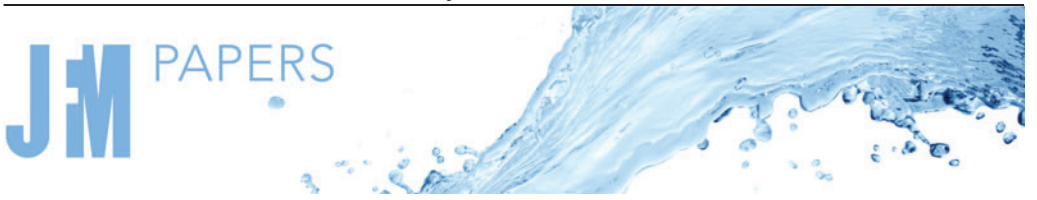

Instability evolution of a shock-accelerated thin heavy fluid layer in cylindrical geometry

Ming Yuan[1], Zhiye Zhao[1],†, Luoqin Liu[1], Pei Wang[2], Nan-Sheng Liu[1] and Xi-Yun Lu[1]

[1]Department of Modern Mechanics, University of Science and Technology of China, Hefei, Anhui 230026, PR China

[2]Institute of Applied Physics and Computational Mathematics, Beijing 100094, PR China

(Received 18 February 2023; revised 4 July 2023; accepted 4 July 2023)

Instability evolutions of shock-accelerated thin cylindrical SF_6 layers surrounded by air with initial perturbations imposed only at the outer interface (i.e. the 'Outer' case) or at the inner interface (i.e. the 'Inner' case) are numerically and theoretically investigated. It is found that the instability evolution of a thin cylindrical heavy fluid layer not only involves the effects of Richtmyer–Meshkov instability, Rayleigh–Taylor stability/instability and compressibility coupled with the Bell–Plesset effect, which determine the instability evolution of the single cylindrical interface, but also strongly depends on the waves reverberated inside the layer, thin-shell correction and interface coupling effect. Specifically, the rarefaction wave inside the thin fluid layer accelerates the outer interface inward and induces the decompression effect for both the Outer and Inner cases, and the compression wave inside the fluid layer accelerates the inner interface inward and causes the decompression effect for the Outer case and compression effect for the Inner case. It is noted that the compressible Bell model excluding the compression/decompression effect of waves, thin-shell correction and interface coupling effect deviates significantly from the perturbation growth. To this end, an improved compressible Bell model is proposed, including three new terms to quantify the compression/decompression effect of waves, thin-shell correction and interface coupling effect, respectively. This improved model is verified by numerical results and successfully characterizes various effects that contribute to the perturbation growth of a shock-accelerated thin heavy fluid layer.

Key words: shock waves

† Email address for correspondence: zzy12@ustc.edu.cn

1. Introduction

The instability that occurs at the interface between two fluids with different densities due to the persistent acceleration of the light fluid to the heavy fluid is referred to as the Rayleigh–Taylor (RT) instability (Rayleigh 1883; Taylor 1950). The Richtmyer–Meshkov (RM) instability develops when a shock wave refracts through an interface between two fluids with different densities (Richtmyer 1960; Meshkov 1969). These two instabilities have been widely encountered as playing key roles in various topics, including geological flows (Houseman & Molnar 1997), astrophysical flows (Bell *et al.* 2004; Hester 2008), magnetic fields (Isobe *et al.* 2005), chemical reactions (Chertkov, Lebedev & Vladimirova 2009), nuclear fusion (Lindl *et al.* 2014), material strength (Buttler *et al.* 2012) and explosive detonation (Balakrishnan & Menon 2010). More important applications of RT and RM instabilities can be found in the recent reviews of Zhou *et al.* (2019, 2021). Especially, the evolutions of these two types of interfacial instability are critical for understanding dynamical features of inertial confinement fusion (ICF) (Betti & Hurricane 2016) and supernova explosions (Kane, Drake & Remington 1999). Specifically, the RM instability occurs at the interface of the ablator layer or the fuel layer in an ICF capsule when the shocks generated by intense lasers or X-rays interact with these layers. During the implosion in ICF, RM instability determines the seed of RT instability inducing the mixing that reduces and even eliminates the thermonuclear yield (Kishony & Shvarts 2001). Furthermore, these instabilities also occur in supernovae when the shocks generated by star collapse interact with the multi-layer heavy elements throughout interstellar space (Arnett *et al.* 1989). Then the resultant mixing induced by the RM and RT instabilities shapes the filament structures as in the remnant of the Crab Nebula of 1054 (Hester 2008). Therefore, it is of great significance for scientific research and engineering applications to explore the instability evolution of a shock-accelerated finite-thickness fluid layer.

Compared with previous research about the instability of a single interface (Zhou 2017*a*,*b*), the instability evolution of a fluid layer is more complex due to the presence of two interfaces. The RT instability of a finite-thickness fluid layer was first considered by Taylor (1950), who discovered that the interface coupling effect appears to be significant when the fluid-layer thickness is sufficiently small. Ott (1972) deduced an analytic solution describing the nonlinear evolution of RT instability in a thin fluid layer and explained the formation of bubbles and spikes. Mikaelian (1982, 1985) proposed linear solutions for the perturbation growths induced by RT and RM instabilities on an arbitrary number of stratified fluids. Jacobs *et al.* (1993, 1995) adopted the gas curtain technique to a shocked thin SF_6 layer and observed three specific flow patterns, namely upstream mushrooms, downstream mushrooms and sinuous shape, depending on the initial perturbations on two interfaces. Recently, Liang *et al.* (2020) employed the soap-film technique to examine the instability evolution of an SF_6 layer surrounded by air and confirmed that the flow patterns are determined by the amplitudes and phases of two corrugated interfaces. Later, Liang & Luo (2021) pointed out that finite-thickness fluid-layer evolution not only involves both the RM and RT instabilities, but also strongly depends on the waves reverberated inside the layer. They first reported that the rarefaction waves inside the fluid layer induce additional RT instability and decompression effect on the first interface, and the compression waves inside the fluid layer cause additional RT stabilization and compression effect on the other interface. Here, the compression/decompression effect is defined as the sudden decrease/increase of perturbation amplitude of the interface impacted by one known wave (Richtmyer 1960; Liang & Luo 2021).

The research work mentioned above focused mainly on planar geometry, but convergent geometries are encountered more commonly in reality, for example ICF (Betti &

Hurricane 2016) and supernovae (Kane *et al.* 1999), and thus are of more practical interest. Cylindrical geometry which involves principal effects of convergent geometries has been widely used as a natural choice to study the convergent effects on interfacial instability evolution (Mikaelian 1990; Hsing & Hoffman 1997; Guo *et al.* 2017; Ding *et al.* 2019; Mikaelian 2005; Sun *et al.* 2020; Zhang *et al.* 2020). According to a previous study (Weir, Chandler & Goodwin 1998), the Bell–Plesset (BP) effect (Bell 1951; Plesset 1954) occurring in cylindrical geometry expands or compresses perturbation scales and alters the perturbation growth characteristics induced by RM and RT instabilities. Epstein (2004) extended the groundbreaking model (Bell 1951) describing the instability growth on a thick cylindrical shell in vacuum to the single cylindrical interface between two uniformly compressing fluids which are compressing at the same rate (i.e. the Atwood number does not change). This compressible Bell model (Epstein 2004) has been verified to well capture not only the RM instability, RT instability and the BP effect but also the compressibility effect referring to the effect of fluid compression caused by the basic flow to the centre of cylindrical geometry (Luo *et al.* 2019; Wu, Liu & Xiao 2021). Recently, the instability evolutions of shock-accelerated cylindrical heavy gas layers with initial perturbations imposed at the outer interface and at the inner interface were examined by Ding *et al.* (2019) and Sun *et al.* (2020), respectively. They increased the layer thickness from 15.0 to 35.0 mm and found that the interface coupling effect was weakening. In addition, the rarefaction wave was observed to occur inside the cylindrical fluid layer and induced the RT instability on the perturbed interfaces in experimental work (Ding *et al.* 2019). Zhang *et al.* (2020) gave, for the first time, the mathematical forms of the interface coupling effect referring to the influence of the perturbation growth at one interface on that at another interface and thin-shell correction for a thin cylindrical incompressible fluid shell in vacuum. They pointed that when $\alpha^n < 6$, where α is the ratio of the radii of the outer interface to inner interface and n is the wavenumber of the perturbed interface, the interface coupling effect and thin-shell correction are significant and thus cannot be neglected.

It can be inferred from the works mentioned above that the instability evolution of a shock-accelerated thin fluid layer in cylindrical geometry is complex, including not only the RM instability, RT instability, compressibility and BP effect, but also the waves reverberated inside the layer, thin-shell correction and interface coupling effect. However, the instability evolution of a shock-accelerated thin cylindrical fluid layer inserted into another fluid is still worthy of further investigation. On the one hand, due to the measurement difficulties caused by the close distance between the two interfaces in a thin fluid layer, α only reaches 1.375 and thus the thin-shell correction and interface coupling effect are negligibly weak in experiments with $n = 6$ (Ding *et al.* 2019; Sun *et al.* 2020). On the other hand, the existing model of Zhang *et al.* (2020) aims at a thin fluid shell in vacuum, so that the effects of the waves reverberated inside the thin layer induced by the incident shock on the instability evolution cannot be described theoretically. In practice, the fuel layer in ICF is thin and α is usually as low as 1.111 (Amendt *et al.* 2002; Betti & Hurricane 2016), which enforces the necessity of numerically and theoretically investigating the instability evolution of a thin fluid layer in cylindrical geometry.

In the present study, the instability evolution of a shock-accelerated thin heavy fluid layer in cylindrical geometry has been studied numerically and theoretically to reveal the underlying physical mechanism of the thin fluid layer. An improved compressible Bell model to characterize various effects that contribute to the perturbation growth of the thin heavy fluid layer is proposed and verified by direct numerical simulation (DNS) of the

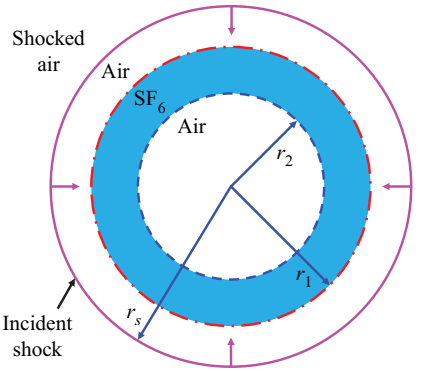

Figure 1. Schematic illustration of a convergent shock impacting a cylindrical SF_6 layer surrounded by air. Here r_1 and r_2 are the radial locations of outer and inner unperturbed interfaces of the SF_6 layer, respectively, and r_s represents the radius of the convergent incident shock.

Species	ρ_i^* (kg m^{-3})	p_i^* (kPa)	T_i^* (K)	γ_i	Pr_i	Sc_i	M_i^* (g mol^{-1})	$\mu_{0,i}^*$ (kg m^{-1} s^{-1})
SF_6	5.98	101.325	298	1.09	0.80	0.691	146.06	1.2388×10^{-5}
Air	1.18	101.325	298	1.40	0.72	0.757	28.96	1.7161×10^{-5}
CO_2	1.80	101.325	298	1.31	0.77	0.766	44.01	1.3711×10^{-5}
H_2	0.08	101.325	298	1.41	0.69	0.686	2.02	0.8377×10^{-5}

Table 1. Initial parameters of the unshocked species. Here the subscript $i = S, A, C$ and H representing the species SF_6, air, CO_2 and H_2, respectively.

Navier–Stokes equations. The remainder of this paper is organized as follows. The DNS strategy used to simulate the instability evolution is described in § 2. The general features of the instability evolution and the improved model describing the perturbation growth along with the relevant results are discussed in § 3. Finally the conclusions are addressed in § 4.

2. Numerical simulations

2.1. *Governing equations*

Direct numerical simulation has been performed on the hydrodynamic instability in cylindrical geometry to study the instability evolution of the shock-accelerated thin heavy fluid layer. Considering the convergent shock to accelerate an SF_6 (sulphur hexafluoride) layer surrounded by air (see figure 1), the pressure p_A^* and density ρ_A^* of unshocked air are chosen as the characteristic scales and are listed in table 1. Here, the characteristic velocity and temperature are described, respectively, as $u_A^* = \sqrt{p_A^*/\rho_A^*}$ and $T_A^* = p_A^* M_A^*/(R^* \rho_A^*)$ with the universal gas constant R^* and molar mass of air M_A^*. Hereafter, the superscript '$*$' denotes dimensional physical quantities and the subscript 'A' corresponds to the quantities of unshocked air. The radius of the unperturbed outer interface of the SF_6 layer r_o^* is used as the characteristic length. Thus, the non-dimensionalized governing equations in cylindrical coordinates (r, θ) are

$$\frac{\partial \rho}{\partial t} + \nabla \cdot (\rho \boldsymbol{u}) = 0, \tag{2.1}$$

$$\frac{\partial(\rho \boldsymbol{u})}{\partial t} + \nabla \cdot (\rho \boldsymbol{u}\boldsymbol{u}) = -\nabla p + \frac{1}{Re}\nabla \cdot \boldsymbol{\tau}, \tag{2.2}$$

$$\frac{\partial(\rho E)}{\partial t} + \nabla \cdot [(\rho E + p)\boldsymbol{u}] = \frac{1}{Re}\nabla \cdot (\boldsymbol{\tau} \cdot \boldsymbol{u}) - \frac{1}{RePr}\nabla \cdot \boldsymbol{q}_c - \frac{1}{ReSc}\nabla \cdot \boldsymbol{q}_d, \tag{2.3}$$

$$\frac{\partial(\rho Y_A)}{\partial t} + \nabla \cdot (\rho Y_A \boldsymbol{u}) = -\frac{1}{ReSc}\nabla \cdot \boldsymbol{J}_A, \tag{2.4}$$

where ρ is the fluid density; $\boldsymbol{u} = (u_r, u_\theta)$ denotes the velocity vector; p is the pressure; $E = C_v T + \boldsymbol{u} \cdot \boldsymbol{u}/2$ denotes the specific total energy with C_v being the specific heat at constant volume and T the temperature; $Y_A = \rho_A/\rho$ is the species mass fraction of air and $Y_S = 1 - Y_A$ is the species mass fraction of SF_6; and the symbol ∇ denotes the vector-differentiation operator. The stress tensor is obtained as $\boldsymbol{\tau} = 2\mu \boldsymbol{S} - 2\mu/3(\nabla \cdot \boldsymbol{u})\boldsymbol{\delta}$, where μ is the dynamic viscosity, $\boldsymbol{S} = (\nabla \boldsymbol{u} + (\nabla \boldsymbol{u})^T)/2$ is the strain-rate tensor and $\boldsymbol{\delta}$ represents the unit tensor. The heat fluxes due to heat conduction ($\boldsymbol{q}_c$) and interspecies enthalpy diffusion ($\boldsymbol{q}_d$) are given by $\boldsymbol{q}_c = -\gamma_A/[M_A(\gamma_A - 1)]\kappa \nabla T$ and $\boldsymbol{q}_d = \sum h_i \boldsymbol{J}_i$ ($i = A, S$), respectively, where γ_A is the ratio of specific heats of air, M_A is the molar mass of air, κ is the heat conduction coefficient, h_i is the enthalpy, $\boldsymbol{J}_i = -\rho D \nabla Y_i$ is the diffusive mass flux obtained by the Fick law and D is the diffusion coefficient. The above governing equations are closed with the non-dimensionalized ideal gas equation of state, i.e. $p = \rho T/M$, where M is the molar mass.

Following recent work (Ge *et al.* 2020), the density and pressure of the mixture are obtained by the summation of each species, while the temperature is equal for each species of the mixture. Therefore, the molecular mass of the mixture is given by $M = (\sum Y_i/M_i)^{-1}$, where M_i is the molecular mass of the ith species. The quantities describing the physical properties of the mixture, such as the dynamic viscosity μ, the diffusion coefficient D, the heat conduction coefficient κ, the specific heat at constant pressure C_p and the specific heat at constant volume C_v, are calculated by the linear combinations of each species weighted with their mass fractions (Ge *et al.* 2020). The dynamic viscosity of the ith species μ_i is computed by the Sutherland law as

$$\mu_i = \frac{\mu^*_{0,i}}{\mu^*_A}\left(\frac{TT^*_A}{T^*_0}\right)^{3/2}\frac{T^*_0 + T^*_s}{TT^*_A + T^*_s}, \tag{2.5}$$

where $T^*_s = 124\,\mathrm{K}$ and $\mu^*_{0,i}$ is the dynamic viscosity at the reference temperature $T^*_0 = 273.15\,\mathrm{K}$. The heat conduction coefficient κ_i and diffusion coefficient D_i of the ith species can be obtained by the constant Prandtl number, $Pr_i = C^*_{p,i}\mu^*_i/\kappa^*_i$, and the constant Schmidt number, $Sc_i = \mu^*_i/(\rho^*_i D^*_i)$, respectively. The specific heat at constant pressure can be calculated by $C^*_{p,i} = \gamma_i R^*/[(\gamma_i - 1)M^*_i]$. In that, the parameters of SF_6 and air to obtain the quantities describing the mixture properties are listed in table 1.

The non-dimensional parameters in (2.1)–(2.4) are the Reynolds, Prandtl and Schmidt numbers defined, respectively, as

$$Re = \frac{\rho^*_A u^*_A r^*_o}{\mu^*_A}, \quad Pr = \frac{C^*_{p,A}\mu^*_A}{\kappa^*_A}, \quad Sc = \frac{\mu^*_A}{\rho^*_A D^*_A}. \tag{2.6a–c}$$

In the present study, the physical quantities of unshocked air are chosen as the characteristic scales. Thus the Prandtl and Schmidt numbers in governing equations are 0.72 and 0.757, respectively. The Reynolds number Re here is set as 10^5 for which the corresponding Reynolds number based on the perturbation wavelength and the post-shock Richtmyer velocity is $2300 \gg 256$. Therefore, according to Walchli & Thornber (2017),

the instability evolution satisfies the inviscid solution. This indicates that the viscosity, heat conduction and species diffusion have insignificant effects on the perturbation growth of the cases in our study.

2.2. *Numerical algorithms and validation*

A numerical algorithm of high-order finite difference schemes is used to solve the governing equations (2.1)–(2.4) in cylindrical coordinates (Zhao *et al.* 2021; Fu *et al.* 2022). Specifically, the seventh-order weighted essentially non-oscillatory scheme is implemented to discretize the convective terms. The eighth-order central difference scheme is performed to discretize the viscous terms. The time derivative is approximated by the classical third-order Runge–Kutta method.

To validate the present algorithm, an initially unperturbed air–SF_6 interface accelerated by a convergent shock wave in cylindrical geometry is simulated. This simulation is a limit example of a cylindrical shock wave accelerating a heavy fluid layer, namely the case that the radius of the inner interface of the SF_6 layer r_2 in figure 1 is zero. This validation example also includes the evolution of the cylindrical interface, the motion of the converging shock wave and the interaction between the shock wave and interface, which are similar to the fluid layer problem considered here, and has accurate experimental (Lei *et al.* 2017) and numerical (Wu *et al.* 2021) data for verification. Consistent with experiment (Lei *et al.* 2017), ambient air mixed with SF_6 (mass fraction of air is 97.5 %) and the inside SF_6 mixed with air (mass fraction of SF_6 is 94.5 %) are set, and the obtained trajectories of the interface and shock wave are compared in figure 2. The temporal trajectories of the present simulation are in good agreement with the data of Lei *et al.* (2017) and Wu *et al.* (2021), ensuring that the present DNS is reliable for resolving the complicated interaction between the interface and shock wave.

2.3. *Problem set-up*

To study the instability evolution of the shock-accelerated thin heavy fluid layer, the model problem that a convergent shock wave impacts a cylindrical SF_6 layer surrounded by air is set as shown in figure 1. The ratio of the radial positions of the outer to inner interfaces of the SF_6 layer, i.e. $\alpha = r_1/r_2$, is defined to characterize the layer thickness. For convenience, the quantities at the outer and inner interfaces are denoted by subscripts 1 and 2, respectively. In the present study, the initial ratio α_0 has been set as 1.111 and the SF_6 layer is thin enough to have an obvious interface coupling effect (Zhang *et al.* 2020). By introducing the error function to smooth the interfaces, the mass fraction field of air is initialized as

$$Y_A(r, \theta; t = 0) = \frac{1}{2}\left[2 + \mathrm{erf}\left(\frac{r - \zeta_1(\theta)}{\delta}\right) - \mathrm{erf}\left(\frac{r - \zeta_2(\theta)}{\delta}\right)\right], \tag{2.7}$$

where the initial premixed thickness of the interface δ is set as 0.005, which is low enough to ignore the effect of initial interface diffusion (Walchli & Thornber 2017), and $\zeta_i(\theta)$ $(i = 1, 2)$ is the shape function of the interface. For an unperturbed interface, $\zeta_i(\theta) = r_i$. For a single-mode cosine perturbation, $\zeta_i(\theta) = r_i + a_i \cos(n\theta)$, where a_i is the initial amplitude and n is the number of perturbation waves. The incident shock with shock Mach number $Ma = 1.25$ is initially at $r_s = 1.25$. We assume a uniform pressure $p = 1$ and temperature $T = 1$ in unshocked regions. Note that the main flow after the converging shock is not uniform (Chisnell 1998). Nevertheless, the instability evolution induced by the collision of the converging shock generated by uniform initialization with the perturbed interface is

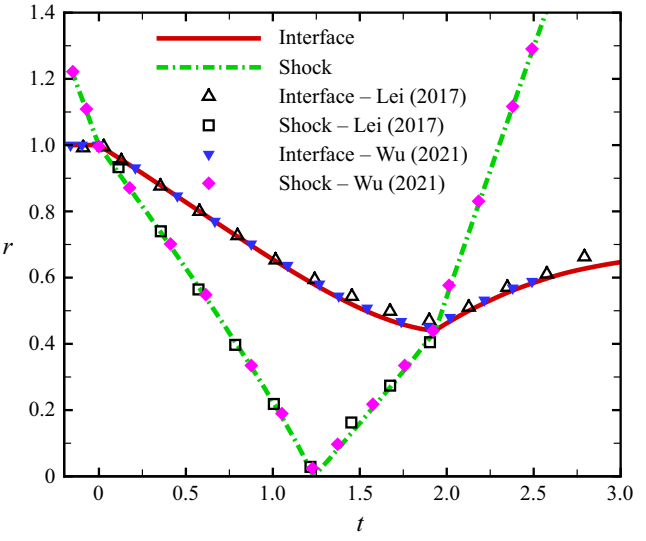

Figure 2. Validation based on simulation of an initially unperturbed air–SF_6 interface impinged by a convergent shock wave. Here comparisons are performed for the positions of the interface and shock wave versus time t. The open and filled symbols represent the experimental (Lei *et al.* 2017) and numerical (Wu *et al.* 2021) data, respectively. The lines denote the present results.

in good agreement with the experimental result and thus the initial non-uniform effect on the instability growth is insignificant (Wu *et al.* 2021; Li *et al.* 2022). Therefore, according to previous treatments (Li *et al.* 2021; Wu *et al.* 2021; Li *et al.* 2022; Yan *et al.* 2022), the initial state in post-shock regions is supposed to be uniform and calculated as

$$\rho_s = \frac{(\gamma_A+1)Ma^2}{2+(\gamma_A-1)Ma^2}, \quad p_s = \frac{2\gamma_A Ma^2-\gamma_A+1}{\gamma_A+1}, \quad u_{r,s} = -\frac{2\gamma_A^{1/2}(Ma^2-1)}{(\gamma_A+1)Ma}, \tag{2.8a–c}$$

using the Rankine–Hugoniot conditions.

As depicted in figure 1, the shock-accelerated thin SF_6 layer is simulated within a two-dimensional circular domain $D = \{(r,\theta)|r_{in} \leqslant r \leqslant r_{out}, 0 \leqslant \theta < 2\pi\}$. To avoid a pole singularity at the centre of cylindrical coordinates, a micro-hole with a radius $r_{in} = 0.01$ is dug out according to Zhao *et al.* (2020) and Wu *et al.* (2021). This commonly used strategy has been verified to have little influence on the interfacial instability evolution. In addition, in order to eliminate effects of reflected waves from the exterior boundary, a sufficiently long sponge layer with a radial width of approximately $19r_{out}$ is added at $r > r_{out} = 1.5$. The wall boundary and non-reflecting boundary conditions are applied to the interior and exterior sides, respectively, following previous settings (Wu *et al.* 2021).

3. Results and discussion

3.1. *Initially unperturbed interfaces for thin SF_6 layer*

To provide a base flow, a thin cylindrical SF_6 layer ($\alpha_0 = 1.111$) with initially unperturbed interfaces impacted by a concentric shock is first examined. The wave propagation and interface motions are visualized in figure 3. Note that the temporal origin is defined as the moment when the incident shock meets the outer interface. At the early moment ($t = -0.042$), both the cylindrical incident shock (IS_0) and interfaces of the SF_6 layer

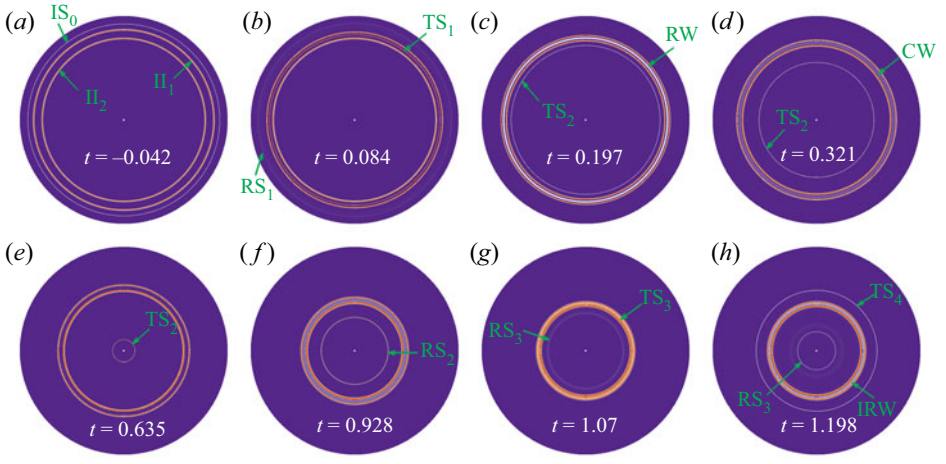

Figure 3. (*a–h*) Wave propagation visualized by $|\nabla\rho|$ contours for the case that the convergent incident shock IS_0 impacts the unperturbed thin SF_6 layer with $\alpha_0 = 1.111$.

are clearly identified in figure 3(*a*). As the IS_0 moves inward and collides with the outer interface II_1 (air–SF_6), the IS_0 bifurcates into an outward-moving reflected shock (RS_1) and an inward-moving transmitted shock (TS_1) as shown in figure 3(*b*). After that, the TS_1 collides with the inner interface II_2 (SF_6–air) and generates a second inward-moving transmitted shock (TS_2) and an outward-moving rarefaction wave (RW). Ascribed to the non-uniform flow field in the convergent geometry (Lombardini, Pullin & Meiron 2014), the RW formed here remains sharp like a shock wave, which is consistent with the experimental results of Ding *et al.* (2019) and Sun *et al.* (2020). After impinging on the II_1, the RW reflects to form an inward-moving compression wave (CW) to collide with the II_2 as shown in figure 3(*d*). However, the formation of the CW and its collision with the II_2 are not presented in the experimental results with a larger radius ratio of $\alpha_0 = 1.833$ obtained by Ding *et al.* (2019) and Sun *et al.* (2020). This observation is attributed to the fact that the SF_6 layer is not thin enough in the experiment so that the reflected shock wave generated in the geometric centre impacts the SF_6 layer soon after the RW impinges the II_1. Due to the impact of the IS_0 on the SF_6 layer, the II_1 and II_2 move towards the geometric centre as shown in figure 3(*c–f*). As the TS_2 reaches the geometric centre, a reflected shock (RS_2) is generated immediately and moves outward away from the centre (see figure 3*f*). Later, the RS_2 impacts the II_2, which is called reshock, a well-known flow phenomenon happening in the convergent RM instability (Lombardini *et al.* 2014; Wu *et al.* 2021). Consequently, the RS_2 bifurcates into an outward-moving transmitted shock (TS_3) and an inward-moving reflected shock (RS_3). Soon, the TS_3 colliding with the II_1 generates an outward-moving transmitted shock (TS_4) and reflects an inward-moving rarefaction wave (IRW) as shown in figure 3(*h*). It is clearly seen in figure 3(*g*,*h*) that both the II_1 and II_2 move outward after reshock.

The quantitative descriptions for the positions of waves and interfaces and for the radial velocities (u_r) of interfaces are displayed in figure 4. These descriptions are useful for the prediction of RT-unstable or RT-stable scenarios at the perturbed interfaces, depending on the interface type and acceleration direction of the interface (Lombardini *et al.* 2014). Specifically, for the II_1 where the light fluid is placed outside, the interface is RT-unstable if it accelerates inward or decelerates outward (i.e. $\ddot{r}_1 < 0$); for the II_2 where the light

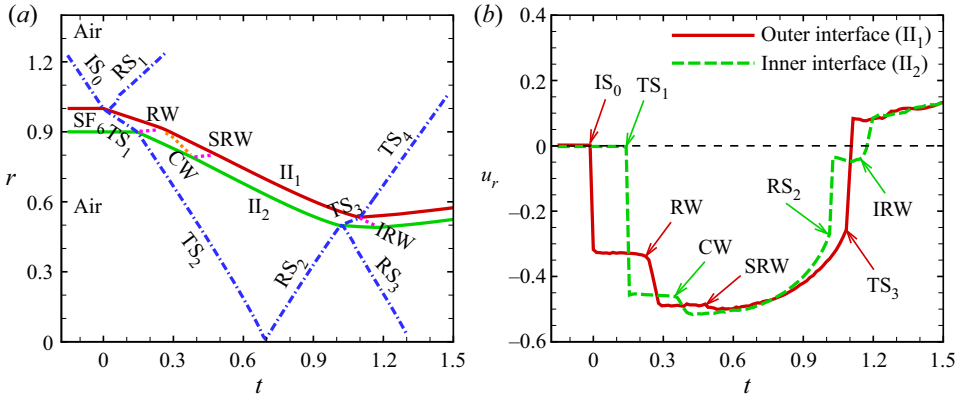

Figure 4. Temporal variations of (*a*) the radial positions of interfaces and waves and of (*b*) the radial velocities of interfaces for the case that the convergent incident shock IS_0 impacts an unperturbed SF_6 layer with $\alpha_0 = 1.111$. Notation: II_1, outer interface; II_2, inner interface; RS_i, ith reflected shock; TS_i, ith transmitted shock; RW, rarefaction wave; CW, compression wave; SRW, second rarefaction wave; IRW, inward-moving rarefaction wave.

fluid is inside, RT-unstable regions correspond to the interface decelerating inward or accelerating outward (i.e. $\ddot{r}_2 > 0$). As presented in figure 4(*a*), the II_1 and II_2 move inward from the static state immediately after being impacted by the IS_0 and TS_1, respectively. The collisions of the TS_3 with II_1 and the IRW with II_2 cause the interfaces to move outward. The radial velocities of the outward-moving interfaces are obviously slower than those of the inward-moving interfaces, which is the same as the experimental results (Ding *et al.* 2019; Sun *et al.* 2020). Furthermore, the temporal variations of the interfacial radial velocities are examined in figure 4(*b*). Three and two steps of u_r appear before reshock as induced by the collisions of waves with the II_1 and II_2, respectively, and the differences of these steps of u_r are listed in table 2. It is worth noting that the RW and CW obviously accelerate the II_1 and II_2 inward, and at this stage the perturbed II_1 and II_2 are RT-unstable and RT-stable, respectively. As displayed in figure 4(*b*), the II_1 has a third small velocity step at $t \approx 0.5$ when the second rarefaction wave (SRW) generated by the collision of the CW on II_2 impinges on II_1. However, the SRW is too weak to be identified via numerical schlieren images. The above phenomenon indicates that the waves generated by the incident shock wave sweeping through the thin SF_6 layer are critical in determining the interfacial radial velocities of the fluid layer. After $t \approx 0.7$, the II_1 and II_2 decelerating inward are RT-stable and RT-unstable, respectively. When the RS_2 and TS_3 impact the II_2 and II_1, respectively, the radial velocities of the inner and outer interfaces have sudden positive increases and their increase extents are listed in table 2. To clearly show the strength of the shocks impacting the interfaces, the shock Mach numbers of the incident shock colliding with the II_1 and II_2, and the shock Mach numbers of the reshock impacting the II_1 and II_2 are listed in table 2. At $t \approx 1.2$, as the IRW generated by the TS_3 impacting II_1 impinges the II_2, the radial velocity of the II_2 has another step and then both the II_1 and II_2 slowly move outward. The present results show the main features of the base flow of the convergent shock accelerating a thin heavy fluid layer, and will facilitate the analysis of the development of a perturbed layer.

Interface	ΔV_1	ΔV_2	ΔV_3	ΔV_r	Ma_i	Ma_r
II_1(air–SF_6)	−0.330	−0.156	−0.014	0.347	1.286	1.383
II_2(SF_6–air)	−0.457	−0.054	—	0.235	1.419	1.236

Table 2. Detailed parameters corresponding to the base flow. Here ΔV_i is the difference of the ith step of u_r before reshock and ΔV_r denotes the difference of u_r induced by reshock; Ma_i refers to the shock Mach number of incident shock colliding with the II_1 and II_2; and Ma_r refers to the shock Mach number of reshock colliding with the II_1 and II_2.

3.2. *Instability evolution of the perturbed thin SF_6 layer*

Next, two typical cases of the perturbed thin SF_6 layer with $\alpha_0 = 1.111$, namely the 'Outer' case consisting of a cosinoidal outer interface and a circular inner interface and the 'Inner' case where the unperturbed outer interface and cosinoidal inner interface are composed, are examined to investigate the instability evolution of the thin heavy fluid layer. The perturbation wavenumber of these two cases is set as $n = 6$, which is consistent with the previous experimental setting (Ding *et al.* 2019; Sun *et al.* 2020). The initial amplitude of the perturbed outer interface for the Outer case is $a_1 = 0.02\lambda_1$, where $\lambda_1 = 2\pi r_1/n$ is the perturbation wavelength of the II_1. Considering that the collision of a shock wave from heavy to light fluids on the perturbed interface causes reverse growth of the perturbation, the initial amplitude of the perturbed inner interface for the Inner case is set as $a_2 = -0.02\lambda_2$, with $\lambda_2 = 2\pi r_2/n$ denoting the perturbation wavelength of the II_2, to ensure that the perturbation growth is in phase with that in the Outer case. The simulations are carried out on three grids of size 600^2 (coarse), 900^2 (intermediate) and 1200^2 (fine), which are uniform in both radial and circumferential directions, and evolutions for the perturbation amplitudes are displayed in figure 5. The perturbation amplitude η_i is defined as $\eta_i = (r_{\theta=0} - r_{\theta=\pi/n})/2$ $(i = 1, 2)$, with $r_{\theta=0}$ and $r_{\theta=\pi/n}$ representing the radii of the locations where $Y_A = 0.5$ along $\theta = 0$ and $\theta = \pi/n$ lines, respectively. In this way, the phase reversal in the perturbation growth can be observed (see figure 5*b*). The converged results depicted in figure 5 confirm that the present simulations are reliable for capturing the essential flow dynamics in instability evolution of the shock-accelerated perturbed thin SF_6 layer. In the following, to obtain the fine flow field for the purpose of clear visualization of morphologies of the interfaces and waves, all the discussion of results and analysis concern the simulations of the fine grid resolution (1200^2).

The underlying physical mechanisms of the perturbation growth presented in figure 5(*a*) can be interpreted by the numerical schlieren images for the Outer case shown in figure 6. Initially, the IS_0 together with the II_1 and II_2 can be clearly identified (see figure 6*a*). As the IS_0 moves inward, it first collides with the cosinoidally perturbed II_1, resulting in a perturbed TS_1 moving inward and a perturbed RS_1 moving outward, and both the TS_1 and RS_1 have the same phase as the II_1. It is worth noting that there is a sudden decrease in η_1 at $t = 0$, attributed to the fact that the inward-moving IS_0 first encounters the crest of the II_1 which consequently obtains an inward radial velocity, while the rest of the II_1 remains still. This radial velocity difference produces a sudden decrease of η_1, which is called the compression effect of the IS_0 (Richtmyer 1960). After $t = 0$ when the IS_0 collides with the II_1, the perturbation on the II_1 grows as driven by the RM instability as shown in figure 5(*a*). Later, the TS_1 impacts the II_2 and bifurcates into a perturbed RW in inverse phase with respect to the II_1 and a perturbed TS_2 in the same phase as the II_1 (see figure 6*c*). Due to the TS_1 impacting II_2, a small perturbation is introduced to the II_2 and

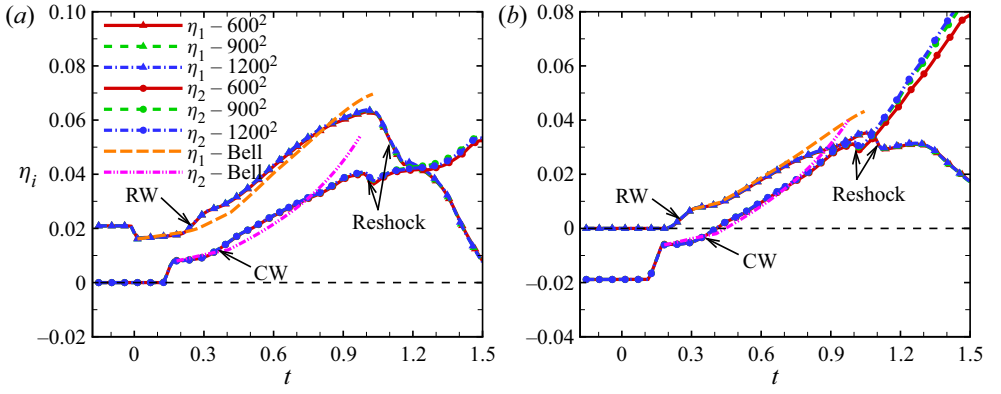

Figure 5. Temporal evolutions of the amplitudes for the perturbed SF_6 layers in (*a*) the Outer case and in (*b*) the Inner case with three grid resolutions: 600^2 (red solid lines), 900^2 (green dashed lines) and 1200^2 (blue dot-dashed lines). The lines with triangles represent the amplitude of the outer interface and lines with circles denote the amplitude of the inner interface. The coloured long-dashed and double-dot-dashed lines are the results calculated by the compressible Bell model (Wu *et al.* 2021).

then grows slowly in the same phase as the II_1 (Zou *et al.* 2019). Specifically, the trough of the inward-moving perturbed TS_1 first encounters the II_2 whose corresponding part consequently obtains an inward radial velocity, while the rest of the II_2 remains still. This radial velocity difference produces a sudden increase of η_2 from $t \approx 0.13$ to $t \approx 0.17$ and thus the TS_1 causes a decompression effect on II_2. After being impinged by the RW, the perturbation on the II_1 has a short-term rapid increase from $t \approx 0.22$ to $t \approx 0.30$ under the decompression effect of the RW. The reasons for the decompression effect of the RW on II_1 are as follows. The RW first encounters the trough of the II_1 whose inward radial velocity is accelerated to a greater value due to the fact that the pressure behind the RW front is lower than that before the RW front (Liang *et al.* 2020). However, the crest of the II_1 still keeps its original radial velocity. This radial velocity difference produces the sudden increase of η_1 from $t \approx 0.22$ to $t \approx 0.30$. Then as shown in figure 6(*d*) the perturbed CW reflected by the collision of the RW on II_1 impacts the II_2, which makes the perturbation on the II_2 increase rapidly. After $t \approx 0.4$ when the CW passes through the II_2, both the II_1 and II_2 move inward and the perturbations increase continuously as driven by the RM instability and the convergence effect (BP effect). It is of interest that the shape of the TS_2 at $t = 0.636$ becomes almost hexagonal with a phase opposite to that at $t = 0.317$. This observation is consistent with the behaviours predicted by Schwendeman & Whitham (1987) using an approximate theory of shock dynamics. As the TS_2 reaches the geometric centre, the outward-moving perturbed RS_2 is generated, and the RS_2 is in phase with respect to the II_2 at $t = 0.931$. After the RS_2 impacts the II_2, the perturbation on the II_2 decreases slightly under the compression effect of the RS_2, and then increases continuously due to the RM instability as shown in figure 5(*a*). Soon, the perturbed TS_3 generated by the RS_2 impacting on II_2 collides with the II_1, and as shown in figure 5(*a*) the perturbation on the II_1 grows in the opposite direction after $t \approx 1.1$ due to the RM instability with the shock travelling from heavy to light fluids. Especially, the spike structure formed on the II_1 grows in a direction opposite to that formed on the II_2 at $t = 1.498$ as presented in figure 6(*i*).

For the Outer case, a very interesting and noteworthy phenomenon in the instability evolution of the thin SF_6 layer is that the inner interface grows in the same phase as the outer interface before the SF_6 layer is re-accelerated by reshock. This behaviour is different

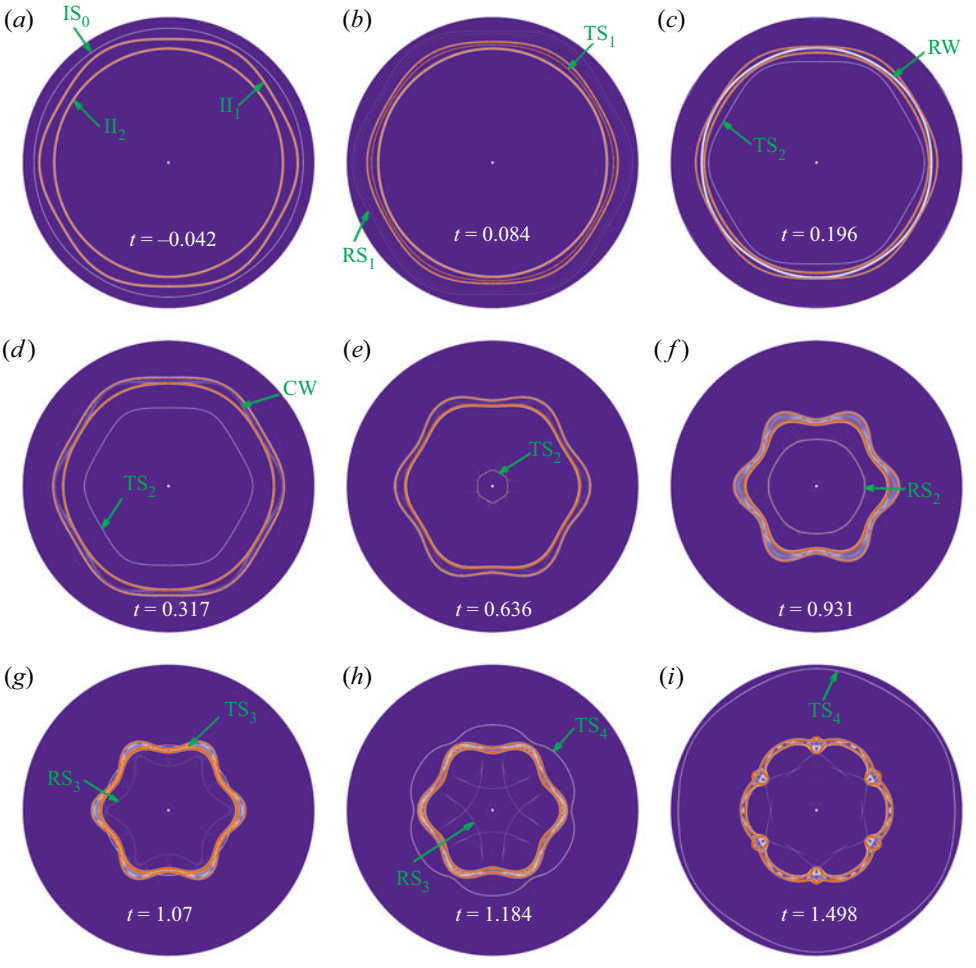

Figure 6. (*a–i*) Wave propagation visualized by the $|\nabla\rho|$ contours for the Outer case.

from the inverse phase growth of the inner interface compared with the outer interface in the instability evolution of the thick SF_6 layer (Ding *et al.* 2019). In order to explain this difference between the cases of the thin and thick fluid layers, it is necessary to clarify the evolution mechanism of the interface after the convergent perturbed shock impacts the circular interface. According to a previous study (Zou *et al.* 2019), the problem of the perturbed shock impacting on the unperturbed interface in convergent geometry is a non-standard RM instability where the baroclinic mechanism is somewhat insignificant. In fact, the pressure perturbation and cylindrical BP effect contribute most significantly to the deformed shock-induced RM instability (Zou *et al.* 2019). To this end, the growth rate of the perturbation amplitude of the II_2 after $t = t_{TS_1}$ when the perturbed TS_1 impacts the II_2 can be expressed as (Zou *et al.* 2019)

$$\dot{\eta}_2 = \varepsilon \frac{|\Delta V_1|}{V_{s,t=t_{TS_1}}} \dot{\eta}_{s,t=t_{TS_1}} + \frac{|\Delta V_1|}{r_2} \eta_{2,t=t_{TS_1}}. \tag{3.1}$$

The first term on the right-hand side of the above equation represents the contribution of the pressure perturbation which can be further divided into impulsive perturbation and

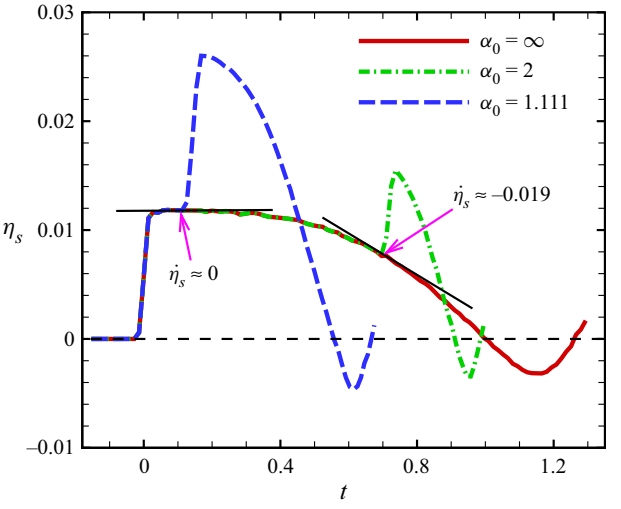

Figure 7. The amplitudes of the TS_1 versus time for the Outer case with $\alpha_0 = 1.111$, $\alpha_0 = 2$ and $\alpha_0 = \infty$ (only the outer interface). The amplitude η_s is defined as $\eta_s = (r_{\theta=0} - r_{\theta=\pi/6})/2$, with $r_{\theta=0}$ and $r_{\theta=\pi/6}$ representing the radial points where the TS_1 intersects with lines $\theta = 0$ and $\theta = \pi/6$, respectively. The tangent lines are given at the moment when the TS_1 impacts the II_2.

continuous perturbation (Zou *et al.* 2019). Here, ε is a dimensionless parameter and $1 - \varepsilon$ stands for the ratio of the continuous perturbation to the impulsive perturbation, ΔV_1 is the radial velocity difference of the II_2 induced by the circular TS_1 and is listed in table 2, $V_{s,t=t_{TS_1}}$ represents the radial velocity of the circular TS_1 at $t = t_{TS_1}$ and $\dot{\eta}_{s,t=t_{TS_1}}$ denotes the perturbation growth rate of the perturbed TS_1 at $t = t_{TS_1}$. The contribution of the cylindrical BP effect is represented by the second term on the right-hand side of (3.1) in which $\eta_{2,t=t_{TS_1}}$ is the amplitude of the perturbation on the II_2 introduced by the TS_1 at $t = t_{TS_1}$ and r_2 denotes the radial location of the II_2. The temporal variation of the amplitude of the TS_1 is plotted in figure 7 to obtain $\dot{\eta}_{s,t=t_{TS_1}}$ in (3.1). It is clearly seen that for the Outer case of the thin SF_6 layer (i.e. $\alpha_0 = 1.111$), $\dot{\eta}_{s,t=t_{TS_1}} \approx 0$, which means that the only contribution of $\dot{\eta}_2$ is from the cylindrical BP effect and is positive. Thus, after being impacted by the TS_1, the II_2 of the thin SF_6 layer keeps the same phase growth as the II_1, and then the perturbed CW accelerating the inward movement of the II_2 makes the perturbation on the II_2 grow rapidly. With the thickening of the initial SF_6 layer, $\dot{\eta}_{s,t=t_{TS_1}}$ decreases gradually and is negative. For example, when $\alpha_0 = 2$, $\dot{\eta}_{s,t=t_{TS_1}} \approx -0.019$. In addition, based on the facts that $\eta_{2,t=t_{TS_1}}$ of the thick SF_6 layer decreases due to the decrease of the perturbation amplitude of the inward-moving TS_1 and that the value of ε in (3.1) is approximately 1 (Zou *et al.* 2019), $\dot{\eta}_2$ of the thick SF_6 layer (i.e. $\alpha_0 = 2$) is dominated by the pressure perturbation and is negative. Therefore, η_2 of the thick SF_6 layer in the same phase at $t = t_{TS_1}$ with η_1 is reversed rapidly at a negative growth rate, and the II_2 and II_1 are in inverse phase. This result is also obtained in previous experimental work (Ding *et al.* 2019).

The acceleration of the shock on the thin SF_6 layer also causes the instability evolution of the interfaces for the Inner case as shown in figure 5(*b*), which can be further examined by the numerical schlieren images in figure 8. Attributed to the II_1 without perturbation, the IS_0, RS_1 and TS_1 still keep a circular shape with no perturbation introduced before the collision of the TS_1 with the cosinoidal II_2. As time proceeds, the TS_1 collides with the II_2, generating a perturbed TS_2 in a phase opposite to that of the initial II_2 and a

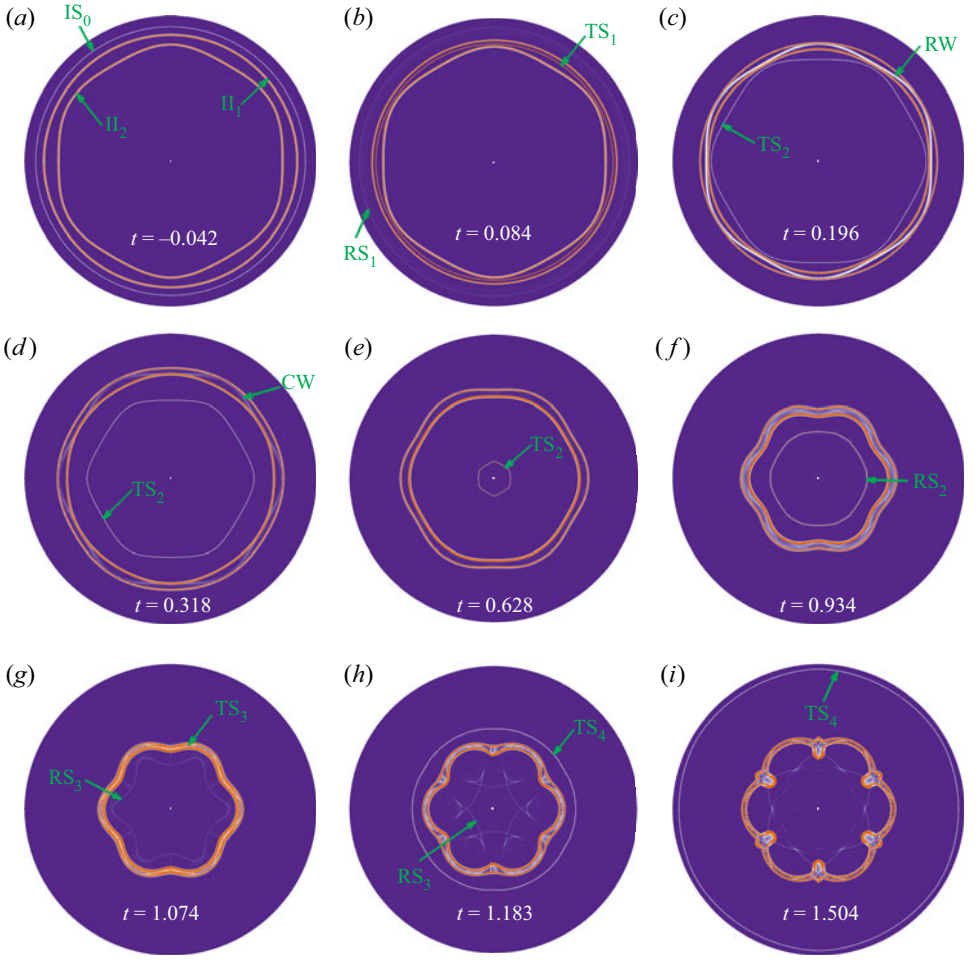

Figure 8. (*a–i*) Wave propagation visualized by the $|\nabla\rho|$ contours for the Inner case.

perturbed RW in the same phase as the initial II_2. The above phenomena were also found in a previous experiment (Sun *et al.* 2020) and the reason for the anti-phase TS_2 is interpreted as follows. The inward-moving TS_1 first encounters the crest of the cosinoidal II_2 and then a part of the TS_1 transmits into the air attaining a higher travelling speed. While the rest of the TS_1 continues to propagate in SF_6 at a lower speed. This radial velocity difference produces an anti-phase perturbation on the TS_2. In addition, due to the impingement of the TS_1 on II_2, the initial negative η_2 has an instantaneous increase at $t \approx 0.15$ under the compression effect of the TS_1, and then grows slowly as driven by the RM instability and BP effect. After the perturbed RW impinging on the II_1, a perturbation amplitude in inverse phase with respect to the RW is introduced on the II_1, and then grows due to the cylindrical BP effect caused by the inward movement of the II_1. However, the impingement of the RW does not obviously cause the instability evolution on the II_1 of the thick SF_6 layer with $\alpha_0 = 1.833$ (Sun *et al.* 2020), due to the reduction of the perturbation on the RW after a long-distance outward movement in the thick fluid layer. Later, the perturbed CW reflecting from the II_1 and moving inward impacts the II_2, speeding up the growth of η_2 so that η_2 increases quickly over zero. After $t \approx 0.4$, the II_1 and II_2 grow in the same phase until the RS_2 reflected from the geometric centre reshocks the SF_6 layer.

The instability evolution after reshock in the Inner case is the same as that in the Outer case, namely the perturbation of the II_2 increases continuously and the perturbation of the II_1 decreases.

For the Outer and Inner cases, the instabilities on both the II_1 and II_2 have a significant increase before reshock. In groundbreaking work, Bell (1951) employed a potential flow model to describe the instability growth on a thick cylindrical shell in vacuum, where the shell can be either incompressible or uniformly compressing. Later, Epstein (2004) extended the Bell model to the fluid–fluid case assuming two uniformly compressing fluids which are compressing at the same rate (i.e. the Atwood number does not change). Here, we examine whether this compressible Bell model capturing well the perturbation growth of the thick cylindrical layer (Ding *et al.* 2019) can describe the instability evolution of the thin SF_6 layer considered here. Under a small-perturbation assumption, the simplified compressible Bell model takes the form (Bell 1951; Epstein 2004)

$$\dot{\eta}_i = \dot{\eta}_{i,RM} + \dot{\eta}_{i,RT} + \dot{\eta}_{i,Com}, \tag{3.2}$$

where the single dot denotes the first derivative with respect to time t, $\dot{\eta}_{i,RM}$ represents the perturbation growth rate due to the RM instability with the BP effect, $\dot{\eta}_{i,RT}$ is the growth rate contributed by the RT stability/instability with the BP effect and $\dot{\eta}_{i,Com}$ denotes the growth rate caused by the compressibility effect that refers to the effect of fluid compression caused by the basic flow to the centre (Epstein 2004; Luo *et al.* 2019). Note that the BP effect is coupled into each of the above terms and difficult to isolate from others (Wu *et al.* 2021). The above three contributions to the perturbation growth rate are expressed as (Epstein 2004; Wu *et al.* 2021)

$$\dot{\eta}_{i,RM} = \frac{r^2_{i,t=t_j^+}\dot{\eta}_{i,t=t_j^+}}{r_i^2(t)}, \tag{3.3a}$$

$$\dot{\eta}_{i,RT} = -\frac{nA_{T,i}+1}{r_i^2(t)}\int_{t_0}^{t} r_i(\tau)\ddot{r}_i(\tau)\eta_i(\tau)\,\mathrm{d}\tau, \tag{3.3b}$$

$$\dot{\eta}_{i,Com} = \frac{c_i}{r_i^2(t)}\left[\int_{t_0}^{t} r_i(\tau)\dot{r}_i(\tau)\eta_i(\tau)\,\mathrm{d}\tau + \int_{t_0}^{t} r_i^2(\tau)\dot{\eta}_i(\tau)\,\mathrm{d}\tau\right]. \tag{3.3c}$$

Here, $i = 1$ and 2 corresponding to the II_1 and II_2, respectively, $r_{i,t=t_j^+}$ and $\dot{\eta}_{i,t=t_j^+}$ represent the position and growth rate of the ith interface at the end moment t_j^+ of the jth wave passing through the interface, respectively, and $A_{T,i} = (\rho_{i,in} - \rho_{i,out})/(\rho_{i,in} + \rho_{i,out})$ is the post-shock Atwood number at the ith interface with $\rho_{i,in}$ and $\rho_{i,out}$ representing the inner and outer fluid densities, respectively. The parameter $c_i = -\dot{\rho}_{i,in}/\rho_{i,in} = -\dot{\rho}_{i,out}/\rho_{i,out}$ in (3.3*c*) characterizes the expansion rate of the species at the ith interface, which can be approximated as a constant value, $c_i \approx [(r_{i,min}/r_{i,0})^2 - 1]/t_{res}$ (Luo *et al.* 2019; Wu *et al.* 2021). Here, $r_{i,min}$ denotes the smallest radius of the ith interface during its motion, $r_{i,0}$ is the initial position of the ith interface and t_{res} represents the time when the reshock happens. Note that the significant deviations between the compressible Bell model and the DNS results before reshock are presented in figure 5, and the reasons of these deviations are as follows. On the one hand, the compression/decompression effect of the impingement of the waves on the interface cannot be described by the compressible Bell model. For example, in the Outer case, this model fails to capture the rapid increase of η_1 when $t \approx 0.22 \sim 0.30$ under the decompression effect of the RW. On the other hand, attributed to

the fact that $\alpha^n < 6$ ($\alpha = r_1/r_2$) in the present study, the interface coupling effect and thin-shell correction are critical to the perturbation growth and must be considered (Zhang *et al.* 2020). Therefore, the neglect of the interface coupling effect and thin-shell correction also makes the compressible Bell model deviate from the DNS results.

3.3. *Model for the instability evolution of the thin SF_6 layer*

According to the detailed analysis in the previous subsection, improvement in the compressible Bell model is required to capture the instability evolution of the thin heavy fluid layer, by including new terms to describe the contributions of interface coupling effect, thin-shell correction and compression/decompression effect of waves. Based on the potential flow theory, Zhang *et al.* (2020) gave for the first time the mathematical forms of the interface coupling effect and thin-shell correction for a thin cylindrical incompressible fluid shell in vacuum, which are included in the equations for η_1 and η_2 as (Zhang *et al.* 2020)

$$\frac{\mathrm{d}(r_1^2\dot{\eta}_1)}{\mathrm{d}t} + (n+1)\ddot{r}_1 r_1 \eta_1 + \frac{2n}{\alpha^{2n}-1}\ddot{r}_1 r_1 \eta_1 = \frac{2n\alpha^{n+1}}{\alpha^{2n}-1}\ddot{r}_1 r_1 \eta_2 + \frac{2n\alpha^{n-1}(\alpha^2-1)}{\alpha^{2n}-1}\dot{r}_1 r_1 \dot{\eta}_2, \tag{3.4}$$

$$\frac{\mathrm{d}(r_2^2\dot{\eta}_2)}{\mathrm{d}t} - (n-1)\ddot{r}_2 r_2 \eta_2 - \frac{2n}{\alpha^{2n}-1}\ddot{r}_2 r_2 \eta_2 = -\frac{2n\alpha^{n-1}}{\alpha^{2n}-1}\ddot{r}_2 r_2 \eta_1 + \frac{2n\alpha^{n-1}(\alpha^2-1)}{\alpha^{2n}-1}\dot{r}_2 r_2 \dot{\eta}_1, \tag{3.5}$$

respectively, where $\alpha = r_1/r_2$ and the dot and double dots denote the first and second derivatives with respect to time t, respectively. The first two terms on the left-hand side of (3.4) and (3.5) represent the incompressible Bell model (Bell 1951), and the temporal integrals of these two terms are exactly the same as (3.2) in which $|A_{T,i}| = 1$ and the terms of compressibility effect are not included. The third terms on the left-hand side of (3.4) and (3.5) represent the thin-shell corrections (Zhang *et al.* 2020). When the thickness of the layer decreases leading to $\alpha \to 1$, the thin-shell correction becomes important. The terms of the interface coupling effect on the right-hand side of (3.4) and (3.5) are roughly of the order of α^{-n} for large α, namely these coupling terms can be ignored for the thick fluid layer. They can be further divided into amplitude coupling terms and velocity coupling terms corresponding to, respectively, the first and second terms on the right-hand side of (3.4) and (3.5) (Zhang *et al.* 2020).

In fact, the above model given by Zhang *et al.* (2020) can be regarded as an extension of the original Bell model (Bell 1951), that is, the coupling terms and thin-shell correction have been added to predict the perturbation growth of the thin fluid layer in vacuum. For the current heavy fluid layer, the density of SF_6 is much higher than that of air and the absolute values of Atwood number are as large as 0.67 close to 1. Based on the small-perturbation assumption under which the perturbation obeys linear growth, the temporal integral forms of the thin-shell correction and the coupling terms in (3.4) and (3.5) are superimposed on (3.2), i.e.

$$\dot{\eta}_i = \dot{\eta}_{i,RM} + \dot{\eta}_{i,RT} + \dot{\eta}_{i,Com} + \dot{\eta}_{i,Thin} + \dot{\eta}_{i,Cou}, \tag{3.6}$$

to improve the compressible Bell model so that it can describe the instability evolution of the thin SF_6 layer. Here, $\dot{\eta}_{i,Thin}$ and $\dot{\eta}_{i,Cou}$ represent the contributions of the thin-shell

correction and the interface coupling effect to the growth rate of the perturbation on the ith interface, respectively. Term $\dot{\eta}_{i,Thin}$ takes the form

$$\dot{\eta}_{i,Thin} = \frac{(-1)^i}{r_i^2(t)} \int_{t_0}^{t} \frac{2n}{\alpha^{2n}(\tau) - 1} \ddot{r}_i(\tau) r_i(\tau) \eta_i(\tau)\, \mathrm{d}\tau, \tag{3.7}$$

and the forms of $\dot{\eta}_{1,Cou}$ and $\dot{\eta}_{2,Cou}$ are expressed as

$$\begin{aligned}\dot{\eta}_{1,Cou} = \frac{1}{r_1^2(t)} \Bigg\{ & \int_{t_0}^{t} \frac{2n\alpha^{n+1}(\tau)}{\alpha^{2n}(\tau) - 1} \ddot{r}_1(\tau) r_1(\tau) \eta_2(\tau)\, \mathrm{d}\tau \\ & + \int_{t_0}^{t} \frac{2n\alpha^{n-1}(\tau)[\alpha^2(\tau) - 1]}{\alpha^{2n}(\tau) - 1} \dot{r}_1(\tau) r_1(\tau) \dot{\eta}_2(\tau)\, \mathrm{d}\tau \Bigg\}\end{aligned} \tag{3.8}$$

and

$$\begin{aligned}\dot{\eta}_{2,Cou} = \frac{1}{r_2^2(t)} \Bigg\{ & - \int_{t_0}^{t} \frac{2n\alpha^{n-1}(\tau)}{\alpha^{2n}(\tau) - 1} \ddot{r}_2(\tau) r_2(\tau) \eta_1(\tau)\, \mathrm{d}\tau \\ & + \int_{t_0}^{t} \frac{2n\alpha^{n-1}(\tau)[\alpha^2(\tau) - 1]}{\alpha^{2n}(\tau) - 1} \dot{r}_2(\tau) r_2(\tau) \dot{\eta}_1(\tau)\, \mathrm{d}\tau \Bigg\},\end{aligned} \tag{3.9}$$

respectively. On the one hand, when $A_{T,1} = 1$ and $A_{T,2} = -1$, (3.6) without the compressibility effect term recovers the model of Zhang *et al.* (2020). On the other hand, with the fluid layer thickening, i.e. $\alpha \to \infty$, (3.6) can be reduced to the compressible Bell model, i.e. (3.2). The above analysis points to that (3.6) can be viewed in physics as a rational combination of the compressible Bell model describing the single interface of arbitrary A_T with the model of Zhang *et al.* (2020) predicting the evolution of the cylindrical fluid layer in vacuum. Therefore, (3.6) needs to satisfy all the three assumptions involved in these two models, i.e. the small-amplitude assumption, potential flow assumption (Epstein 2004; Zhang *et al.* 2020) and uniformly compressing assumption (Epstein 2004).

As shown in figures 6 and 8, the interfaces of the shock-accelerated thin fluid layer are successively impacted by several waves, and the overall variations of the perturbation amplitudes on the interfaces caused by the compression/decompression effects of the successive waves can be obtained by accumulating every rapid decrease/increase of the amplitude induced by each wave. For the compression effect of one known wave, for example, a shock wave compressing a perturbed interface (Richtmyer 1960), the decrease of the amplitude is usually estimated by

$$\eta^+ - \eta^- = -\frac{|\Delta V_W| T_W}{2}, \tag{3.10}$$

where η^+ and η^- are the amplitudes after and before this wave impacting, respectively, ΔV_W represents the radial velocity step of the circular interface caused by this wave and $T_W = 2\eta^-/V_W$ denotes the time for this wave to travel from the interfacial crest to trough with a constant speed V_W (Wu *et al.* 2021). Consequently, it leads to a perturbation compression rate $\eta^+/\eta^- = 1 - |\Delta V_W|/V_W$ (Richtmyer 1960; Meshkov 1969; Wu *et al.* 2021). The accuracy of (3.10) can be verified by the compression rates of the II_1 impacted by the IS_0 in the Outer case and the II_2 collided by the TS_1 in the Inner case. When the IS_0 impacts the II_1 as shown in figure 5(*a*), ΔV_W of the II_1 is ΔV_1 listed in table 2 and V_W of

the IS_0 is 1.480 which is the absolute value of the slope of the IS_0 position curve in figure 4. Thus, the calculated compression rate of the II_1 is 0.777. In addition, because η_1 decreases rapidly from 0.0209 to 0.0161 at $t \approx 0$ when the IS_0 impacts the II_1, the compression rate can also be measured directly as $0.0161/0.0209 \approx 0.770$. Similarly, the compression rate of the II_2 collided by the TS_1 in the Inner case is calculated as 0.319 and directly measured as 0.310. The above compression rates measured directly are very close to those calculated using (3.10), which proves that (3.10) can reliably model the amplitude decrease caused by the compression effect of one known wave. In fact, (3.10) has also been verified and adopted by recent experimental (Ding *et al.* 2017) and numerical (Wu *et al.* 2021) studies. Furthermore, (3.10) can also estimate the amplitude increase under the decompression effect of a wave by replacing the minus sign on the right-hand side of (3.10) with a plus sign (Liang & Luo 2021). Note that the amplitude of the interface varies linearly with time under the compression/decompression effect of a wave, so (3.10) can describe the time-varying compression/decompression effect by replacing the time variable t with T_W (Liang & Luo 2021). To this end, the time-varying compression/decompression effect (Richtmyer 1960; Liang & Luo 2021) including each wave impacting the ith interface $\eta_{i,CD}(t)$ can be modelled as

$$\eta_{i,CD}(t) = \eta_{i,t_0} + \int_{t_0}^{t} \frac{\Delta V(\tau)}{2}\,\mathrm{d}\tau, \tag{3.11}$$

where η_{i,t_0} is the initial amplitude of the ith interface at $t = t_0$. The function $\Delta V(\tau)$ defined in (3.11) represents the radial velocity step of the circular interface at the moment τ, namely if $t_j^- < \tau < t_j^+$, $\Delta V(\tau) = \pm|\Delta V_j|$, otherwise $\Delta V(\tau) = 0$. Here, ΔV_j is the jth radial velocity step listed in table 2, t_j^- and t_j^+ are the beginning and end moments of the jth wave passing through the interface and the operators '+' and '−' before the term $|\Delta V_j|$ represent decompression and compression effects. Parameters t_j^- and t_j^+ can be obtained directly from the numerical results. For example, when the perturbed RW impinges the II_1 in the Outer case, η_1 increases rapidly in the time range from $t \approx 0.22$ to 0.30 under the decompression effect of the RW as shown in figure 5(*a*). Thus, for the RW passing through the II_1, $t_j^- \approx 0.22$ and $t_j^+ \approx 0.30$. The reverberated waves resulting in the compression/decompression effects modelled by (3.11) are caused by the IS_0 impacting the fluid layer. However, (3.6) based on the potential flow assumption appears independent of whether there is an IS_0 and does not involve the process of wave–interface collision. Therefore, (3.6) excludes the compression/decompression effects of the reverberated waves colliding with the interfaces. By adding (3.11) to the temporal integral of (3.6), the compressible Bell model is further improved and the perturbation amplitude η_i of the ith interface of the SF_6 layer can be completed as the following model:

$$\eta_i = \eta_{i,RM} + \eta_{i,RT} + \eta_{i,Com} + \eta_{i,Thin} + \eta_{i,Cou} + \eta_{i,CD}. \tag{3.12}$$

To verify the reliability of the improved compressible Bell model, for the Outer case, the temporal variations of the perturbation amplitudes calculated by the model (3.12) before reshock are presented and compared with the DNS results in figure 9. One should keep in mind that the improved model (3.12) is also based on the small-amplitude assumption adopted by the Bell model and, therefore, is unable to predict large-amplitude growth of perturbation after reshock, i.e. $t \gtrsim 1.0$. Parameters $r_{i,t=t_j^+}$ and $\dot{\eta}_{i,t=t_j^+}$ required to calculate the $\eta_{i,RM}$ term of the model (3.12) according to (3.3*a*) are obtained by DNS results and listed in table 3. Specifically, the contributions of the impingements of the IS_0, RW and

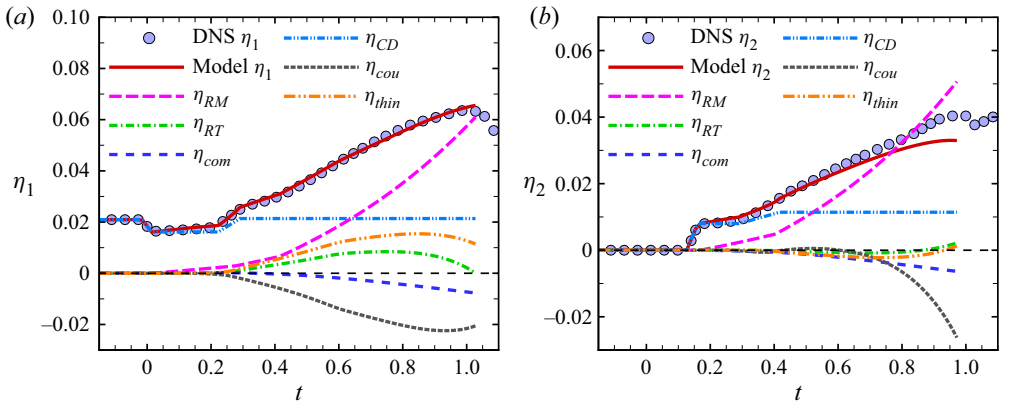

Figure 9. The perturbation amplitudes of the outer (*a*) and inner (*b*) interfaces along with their decomposed contribution terms versus time for the Outer case before reshock. The simulation data marked by symbols are added for comparison.

Interface	t_j^-	t_j^+	$r_{i,t=t_j^+}$	$\dot{\eta}_{i,t=t_j^+}$
II_1	−0.014	0.014	0.995	0.010
II_1	0.223	0.291	0.897	0.025
II_1	—	0.429	0.830	0.058
II_2	0.126	0.168	0.889	0.018
II_2	0.291	0.417	0.772	0.052

Table 3. The parameters required for calculating the terms like $\dot{\eta}_{i,RM}$ and $\eta_{i,CD}$ are obtained by DNS results in the Outer case. Here, t_j^- and t_j^+ are the beginning and end moments of the jth wave passing through the interface and $r_{i,t=t_j^+}$ and $\dot{\eta}_{i,t=t_j^+}$ represent the position and growth rate of the II_i at $t = t_j^+$, respectively.

SRW on the II_1 to the perturbation growth rate are considered, and the contributions of the TS_1 and CW to the perturbation growth rate of the II_2 are taken into account. For the II_1, $A_{T,1}$ required for calculating the term $\eta_{1,RT}$ and c_1 required to calculate the term $\eta_{1,Com}$ are obtained from the base flow as 0.708 and −0.657, respectively. Whereas for the II_2, $A_{T,2} = -0.698$ and $c_2 = -0.776$. The improved compressible Bell model (3.12) agrees well with the DNS result of the II_1 before reshock. For the II_2, the improved model captures well the behaviours of the perturbation growth until $t \approx 0.7$ when the II_2 decelerates inward and then slightly underestimates the DNS results. This underestimation is caused by the thin-shell correction and interface coupling effect which are obtained by the model of Zhang *et al.* (2020) aimed at a thin fluid layer in vacuum. However, compared with the compressible Bell model (3.2), the improved model shows a better prediction of the instability evolution before $t \approx 0.7$.

It is clearly seen in figure 9 that the growths of perturbations on both the II_1 and II_2 are dominated by the RM instability. Term $\eta_{1,RT}$ increases before $t \approx 0.7$ due to the fact that the II_1 is RT-unstable under the inward acceleration of the RW. Attributed to the deceleration of the II_1 and II_2 after $t \approx 0.7$, the II_1 becomes RT-stable and $\eta_{1,RT}$ decreases, while the II_2 is RT-unstable and $\eta_{2,RT}$ increases. This significant difference of $\eta_{1,RT}$ and $\eta_{2,RT}$ is attributed to the interface type (Lombardini *et al.* 2014), i.e. the light–heavy (II_1) and heavy–light (II_2) interfaces. Both $\eta_{1,Com}$ and $\eta_{2,Com}$ decrease

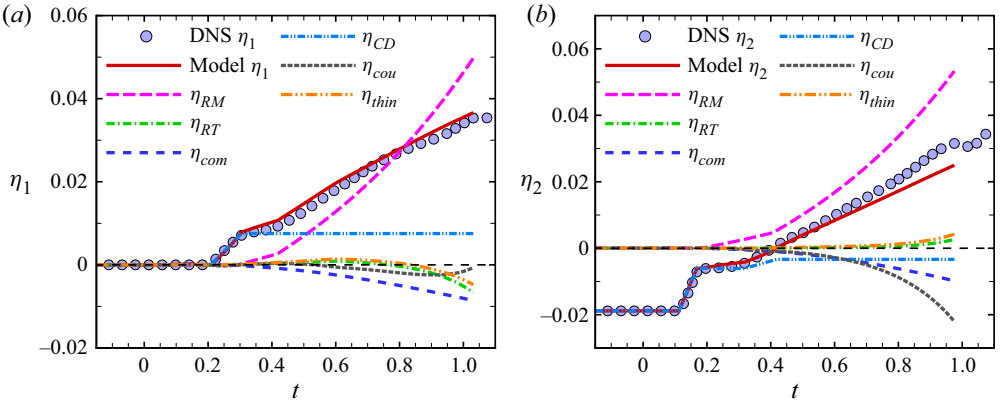

Figure 10. The perturbation amplitudes of the outer (*a*) and inner (*b*) interfaces along with their decomposed contribution terms versus time for the Inner case before reshock. The simulation data marked by symbols are added for comparison.

with time and thus the compressibility effect suppresses the perturbation growth on the interfaces, which is the same behaviour as the experimental result of a shock-accelerated interface in cylindrical geometry (Luo *et al.* 2019). It is particularly important that the thin-shell correction $\eta_{i,Thin}$ and interface coupling effect $\eta_{i,Cou}$ contribute significantly to the instability evolution of the current thin SF_6 layer. The temporal trend of $\eta_{i,Thin}$ behaves similar to that of $\eta_{i,RT}$, resulting from that $\ddot{r}_i r_i \eta_i$ is included in both mathematical forms. However, the contribution of $\eta_{1,Thin}$ in the Outer case is stronger than that of $\eta_{1,RT}$ to the perturbation growth at the II_1 where the initial perturbation is introduced. The interface coupling effect $\eta_{1,Cou}$ suppresses the perturbation growth of the II_1 until $t \approx 0.95$ close to the reshock and then slightly promotes the instability evolution. Nevertheless, the interface coupling effect always suppresses the growth of perturbation on the II_2 before reshock. Note that $\eta_{i,Cou}$ depends on not only the motion of the interface itself (like other terms) but also the perturbation at another interface. Therefore, one could expect that the difference of $\eta_{1,Cou}$ and $\eta_{2,Cou}$ comes from the complex coupling between II_1 and II_2. In addition, $\eta_{i,CD}$ well captures the rapid decrease/increase of perturbation amplitude under the compression/decompression effect of the waves impacting the interfaces. Specifically, the compression effect of the IS_0 causes a sudden decrease of the perturbation on the II_1 at $t \approx 0$ and the decompression effect of the RW at $t \approx 0.25$ leads to an increase of the perturbation on the II_1. For the II_2, the decompression effects of the TS_1 and CW result in increases of perturbation at $t \approx 0.15$ and $t \approx 0.35$, respectively. Note that the decompression effect of the SRW on the II_1 is negligibly weak. Obviously, the great difference of $\eta_{1,CD}$ and $\eta_{2,CD}$ results from that the types of waves colliding with the II_1 and II_2 are different and the collision times are also different.

Furthermore, as shown in figure 10, the improved compressible Bell model is also employed to evaluate the contribution of each effect to the perturbation growth before reshock in the Inner case. Parameters $r_{i,t=t_j^+}$ and $\dot{\eta}_{i,t=t_j^+}$ required to calculate the $\eta_{i,RM}$ term for the Inner case are listed in table 4. Sharing the same base flow, the Inner case has the same $A_{T,i}$ and c_i as the Outer case. As presented in figure 10, the improved compressible Bell model (3.12) also shows a good agreement for the II_1 and for the II_2 before $t \approx 0.7$. The RM instability also dominates the perturbation growth in the Inner case. Because the basic flow is the same for the Outer and Inner cases, both $\eta_{i,RT}$ accounting for the

Interface	t_j^-	t_j^+	$r_{i,t=t_j^+}$	$\dot{\eta}_{i,t=t_j^+}$
II_1	0	0	1	0
II_1	0.210	0.305	0.890	0.020
II_1	—	0.431	0.829	0.050
II_2	0.113	0.169	0.889	0.018
II_2	0.318	0.419	0.771	0.055

Table 4. The parameters required for calculating the terms like $\dot{\eta}_{i,RM}$ and $\eta_{i,CD}$ are obtained by DNS results in the Inner case. Here, t_j^- and t_j^+ are the beginning and end moments of the jth wave passing through the interface and $r_{i,t=t_j^+}$ and $\dot{\eta}_{i,t=t_j^+}$ represent the position and growth rate of the II_i at $t = t_j^+$, respectively.

RT stability/instability and $\eta_{i,Com}$ characterizing the compressibility effect have the same trends of temporal variation in the two cases. In the Inner case, the temporal variation of $\eta_{i,Thin}$ which characterizes the thin-shell correction with similar mathematical form to $\eta_{i,RT}$ is similar to that in the Outer case. Different from the Outer case, the contribution of $\eta_{2,Thin}$ in the Inner case is stronger than that of $\eta_{2,RT}$ to the perturbation growth at the II_2 where the initial perturbation is introduced. In the Inner case, the interface coupling effect also suppresses the instability evolution of the II_1 before $t \approx 0.95$ near reshock and always suppresses the growth of perturbation on the II_2 before reshock, but its contribution is smaller than that in the Outer case. The compression/decompression effect of the waves impinging the interfaces in the Inner case can be observed by $\eta_{i,CD}$. For the II_1, the decompression effect of the RW causes a increase of perturbation at $t \approx 0.25$. For the II_2, the compression effects of the IS_0 and CW lead to decreases of perturbation at $t \approx 0.15$ and $t \approx 0.35$, respectively.

To further validate the present improved model (3.12), the Outer and Inner cases of a shock-accelerated thin CO_2 (carbon dioxide) layer surrounded by H_2 (hydrogen) with initial $|A_{T,i}| = 0.912$ and $n = 12$ are simulated. The parameters for CO_2 and H_2 are listed in table 1. The initial ratio of the radial positions of the outer to inner interfaces α_0 is set as 1.053. It is clearly shown in figure 11 that the present model can also well describe the instability evolution on the CO_2 layer in the Outer and Inner cases. The prediction of the CO_2 layer with initial $|A_{T,i}| = 0.912$ by the model is better than that of the SF_6 layer with initial $|A_{T,i}| = 0.669$, indicating that the present model is more suitable for a heavy fluid layer with large A_T. This is rational as the thin-shell correction and interface coupling effect of the fluid layer in vacuum reduce the accuracy of the model when applied to a fluid layer with low A_T.

4. Concluding remarks

Instability evolution of a shock-accelerated thin SF_6 layer surrounded by air in cylindrical geometry is numerically and theoretically investigated. Two typical cases, namely the Outer and Inner cases with initial perturbations imposed only at the outer and inner interfaces, respectively, are examined in the present study. It is found that both the outer and inner interfaces are unstable for these two cases after the convergent incident shock wave passes through the fluid layer, and the perturbations on the inner and outer interfaces keep growing in the same phase before reshock. The instability evolution of the thin cylindrical heavy fluid layer not only involves the effects of RM instability, RT stability/instability and compressibility coupled with the BP effect, which determine the

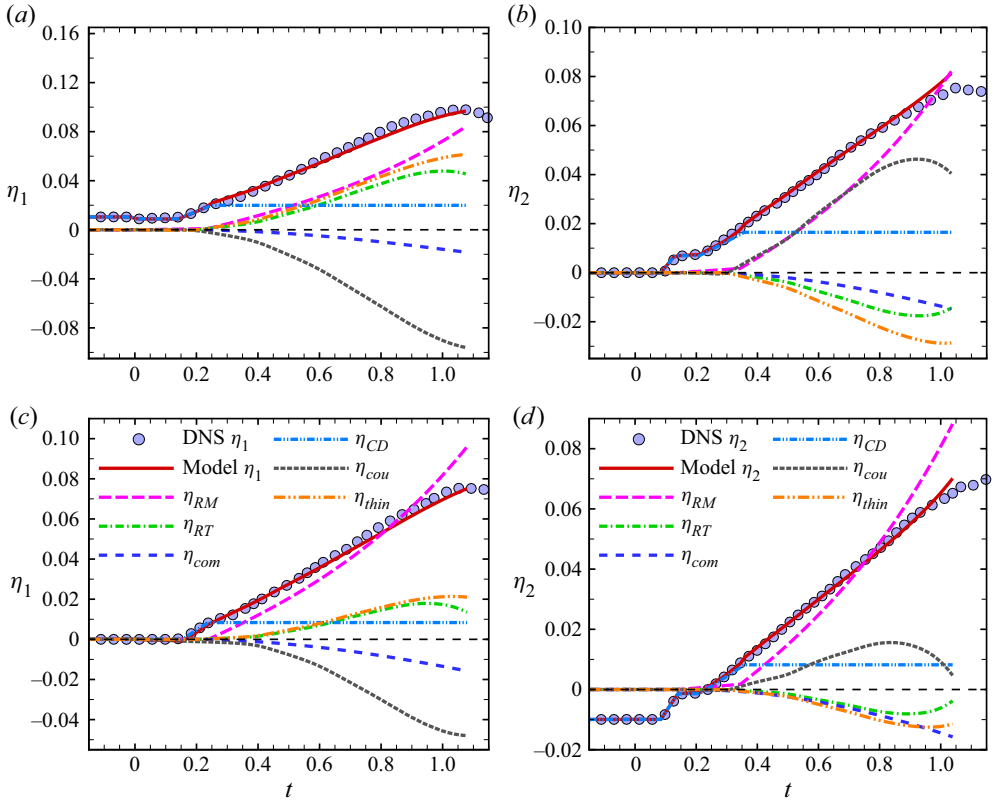

Figure 11. The perturbation amplitudes of the outer (η_1) and inner (η_2) interfaces on the CO_2 layer along with their decomposed contribution terms versus time for the (*a*,*b*) Outer case and (*c*,*d*) Inner case before reshock. The simulation data marked by symbols are added for comparison.

instability evolution of the single cylindrical interface, but also strongly depends on the waves reverberated inside the layer, thin-shell correction and interface coupling effect. Specifically, the RW inside the thin fluid layer accelerates the outer interface inward and induces the decompression effect for both the Outer and Inner cases, and the CW inside the fluid layer accelerates the inner interface inward and causes a decompression effect for the Outer case and a compression effect for the Inner case. It is noted that the compressible Bell model excluding the compression/decompression effect of waves, thin-shell correction and interface coupling effect deviates significantly from the perturbation growth. Furthermore, for the Outer case, different from the inverse growth of the inner interface compared with the outer interface, which is contributed by the pressure perturbation caused by the perturbed transmitted shock wave in the thick fluid layer, the inner interface of the thin fluid layer grows in the same phase as the outer interface under the domination of the cylindrical BP effect.

To reliably describe the instability evolution of the shock-accelerated thin heavy fluid layer in cylindrical geometry, an improved compressible Bell model is proposed, including three new terms to quantify the compression/decompression effect of waves, thin-shell correction and interface coupling effect. Verified by the DNS results, this improved model captures well the behaviours of instability evolutions of outer interface before reshock and of inner interface before $t \approx 0.7$ when the interface decelerates inward.

Via this improved model, various effects that contribute to the perturbation growth of the shock-accelerated thin heavy fluid layer can be characterized successfully. It is shown that the compression/decompression effect of waves inside the fluid layer causes a sudden decrease/increase of the perturbation on the interface. The temporal trend of the thin-shell correction behaves similar to that due to the RT stability/instability effect. The interface coupling effect is found significant in the thin fluid layer, suppressing the instability evolution of the outer interface before $t \approx 0.95$ near reshock and always suppressing the growth of perturbation on the inner interface before reshock. According to the linear superposition principle, the present improved compressible Bell model has its validity straightforwardly in the case with the initial perturbations present at both outer and inner interfaces of a heavy fluid layer. Specifically, such a case can be treated as a linear superposition of the Outer and Inner cases, for which the instability evolutions can be predicted separately by the present model.

Although the present improved model is suitable for a thin heavy fluid layer with large Atwood number due to the employment of the thin-shell correction and interface coupling effect of the thin fluid layer in vacuum, it is extremely important that this improved model theoretically reveals various effects that contribute to the instability evolution of the thin fluid layer, namely the effects of RM instability, RT stability/instability, compressibility, BP effect, thin-shell correction, interface coupling and the waves' compression/decompression. In future work, by generalizing the thin-shell correction and interface coupling effect one can modify the current improved model to describe the instability evolutions of thin fluid layers with arbitrary Atwood number.

Acknowledgements. The authors are very grateful to Dr Y.-S. Zhang at the Institute of Applied Physics and Computational Mathematics for useful discussions on the algorithm and code.

Funding. This work was supported by the National Natural Science Foundation of China (nos 12202436, 11621202, 92052301 and 92252202), by LCP Fund for Young Scholar (no. 6142A05QN22002) and by the Fund of Combustion, Internal Flow and Thermal-Structure Laboratory (no. 6142701210204).

Declaration of interests. The authors report no conflict of interest.

Author ORCIDs.
Ming Yuan https://orcid.org/0000-0002-2602-9990;
Zhiye Zhao https://orcid.org/0000-0003-1509-5084;
Luoqin Liu https://orcid.org/0000-0002-6020-3702;
Nan-Sheng Liu https://orcid.org/0000-0001-9128-1933;
Xi-Yun Lu https://orcid.org/0000-0002-0737-6460.

References

Amendt, P., Colvin, J.D., Tipton, R.E., Hinkel, D.E., Edwards, M.J., Landen, O.L., Ramshaw, J.D., Suter, L.J., Varnum, W.S. & Watt, R.G. 2002 Indirect-drive noncryogenic double-shell ignition targets for the National Ignition Facility: design and analysis. *Phys. Plasmas* **9** (5), 2221–2233.

Arnett, W.D., Bahcall, J.N., Kirshner, R.P. & Woosley, S.E. 1989 Supernova 1987A. *Annu. Rev. Astron. Astrophys.* **27** (1), 629–700.

Balakrishnan, K. & Menon, S. 2010 On turbulent chemical explosions into dilute aluminum particle clouds. *Combust. Theor. Model.* **14** (4), 583–617.

Bell, G.I. 1951 Taylor instability on cylinders and spheres in the small amplitude approximation. *Report No. LA-1321*, LANL.

Bell, J.B., Day, M.S., Rendleman, C.A., Woosley, S.E. & Zingale, M. 2004 Direct numerical simulations of type Ia supernovae flames. II. The Rayleigh–Taylor instability. *Astrophys. J.* **608** (2), 883.

Betti, R. & Hurricane, O.A. 2016 Inertial-confinement fusion with lasers. *Nat. Phys.* **12** (5), 435–448.

BUTTLER, W.T., *et al.* 2012 Unstable Richtmyer–Meshkov growth of solid and liquid metals in vacuum. *J. Fluid Mech.* **703**, 60–84.

CHERTKOV, M., LEBEDEV, V. & VLADIMIROVA, N. 2009 Reactive Rayleigh–Taylor turbulence. *J. Fluid Mech.* **633**, 1–16.

CHISNELL, R.F. 1998 An analytic description of converging shock waves. *J. Fluid Mech.* **354**, 357–375.

DING, J., LI, J., SUN, R., ZHAI, Z. & LUO, X. 2019 Convergent Richtmyer–Meshkov instability of a heavy gas layer with perturbed outer interface. *J. Fluid Mech.* **878**, 277–291.

DING, J., SI, T., YANG, J., LU, X.-Y., ZHAI, Z. & LUO, X. 2017 Measurement of a Richtmyer–Meshkov instability at an air-SF_6 interface in a semiannular shock tube. *Phys. Rev. Lett.* **119** (1), 014501.

EPSTEIN, R. 2004 On the Bell–Plesset effects: the effects of uniform compression and geometrical convergence on the classical Rayleigh–Taylor instability. *Phys. Plasmas* **11** (11), 5114–5124.

FU, C.-Q., ZHAO, Z., XU, X., WANG, P., LIU, N.-S., WAN, Z.-H. & LU, X.-Y. 2022 Nonlinear saturation of bubble evolution in a two-dimensional single-mode stratified compressible Rayleigh–Taylor instability. *Phys. Rev. Fluids* **7** (2), 023902.

GE, J., ZHANG, X.-T., LI, H.-F. & TIAN, B.-L. 2020 Late-time turbulent mixing induced by multimode Richtmyer–Meshkov instability in cylindrical geometry. *Phys. Fluids* **32** (12), 124116.

GUO, H.-Y., WANG, L.-F., YE, W.-H., WU, J.-F. & ZHANG, W.-Y. 2017 Rayleigh–Taylor instability of multi-fluid layers in cylindrical geometry. *Chin. Phys.* B **26** (12), 125202.

HESTER, J.J. 2008 The Crab Nebula: an astrophysical chimera. *Annu. Rev. Astron. Astrophys.* **46** (1), 127–155.

HOUSEMAN, G.A. & MOLNAR, P. 1997 Gravitational (Rayleigh–Taylor) instability of a layer with non-linear viscosity and convective thinning of continental lithosphere. *Geophys. J. Intl* **128** (1), 125–150.

HSING, W.W. & HOFFMAN, N.M. 1997 Measurement of feedthrough and instability growth in radiation-driven cylindrical implosions. *Phys. Rev. Lett.* **78** (20), 3876–3879.

ISOBE, H., MIYAGOSHI, T., SHIBATA, K. & YOKOYAMA, T. 2005 Filamentary structure on the Sun from the magnetic Rayleigh–Taylor instability. *Nature* **434** (7032), 478–481.

JACOBS, J.W., JENKINS, D.G., KLEIN, D.L. & BENJAMIN, R.F. 1995 Nonlinear growth of the shock-accelerated instability of a thin fluid layer. *J. Fluid Mech.* **295**, 23–42.

JACOBS, J.W., KLEIN, D.L., JENKINS, D.G. & BENJAMIN, R.F. 1993 Instability growth patterns of a shock-accelerated thin fluid layer. *Phys. Rev. Lett.* **70** (5), 583–586.

KANE, J., DRAKE, R.P. & REMINGTON, B.A. 1999 An evaluation of the Richtmyer–Meshkov instability in supernova remnant formation. *Astrophys. J.* **511** (1), 335–340.

KISHONY, R. & SHVARTS, D. 2001 Ignition condition and gain prediction for perturbed inertial confinement fusion targets. *Phys. Plasmas* **8** (11), 4925–4936.

LEI, F., DING, J., SI, T., ZHAI, Z. & LUO, X. 2017 Experimental study on a sinusoidal air/SF_6 interface accelerated by a cylindrically converging shock. *J. Fluid Mech.* **826**, 819–829.

LI, J., DING, J., LUO, X. & ZOU, L. 2022 Instability of a heavy gas layer induced by a cylindrical convergent shock. *Phys. Fluids* **34** (4), 042123.

LI, X., FU, Y., YU, C. & LI, L. 2021 Statistical characteristics of turbulent mixing in spherical and cylindrical converging Richtmyer–Meshkov instabilities. *J. Fluid Mech.* **928**, A10.

LIANG, Y., LIU, L., ZHAI, Z., SI, T. & WEN, C.-Y. 2020 Evolution of shock-accelerated heavy gas layer. *J. Fluid Mech.* **886**, A7.

LIANG, Y. & LUO, X. 2021 On shock-induced heavy-fluid-layer evolution. *J. Fluid Mech.* **920**, A13.

LINDL, J., LANDEN, O., EDWARDS, J., MOSES, E. & N.I.C. TEAM 2014 Review of the national ignition campaign 2009–2012. *Phys. Plasmas* **21** (2), 020501.

LOMBARDINI, M., PULLIN, D.I. & MEIRON, D.I. 2014 Turbulent mixing driven by spherical implosions. Part I. Flow description and mixing-layer growth. *J. Fluid Mech.* **748**, 85–112.

LUO, X., LI, M., DING, J., ZHAI, Z. & SI, T. 2019 Nonlinear behaviour of convergent Richtmyer–Meshkov instability. *J. Fluid Mech.* **877**, 130–141.

MESHKOV, E.E. 1969 Instability of the interface of two gases accelerated by a shock wave. *Fluid Dyn.* **4** (5), 101–104.

MIKAELIAN, K.O. 1982 Normal modes and symmetries of the Rayleigh–Taylor instability in stratified fluids. *Phys. Rev. Lett.* **48** (19), 1365–1368.

MIKAELIAN, K.O. 1985 Richtmyer–Meshkov instabilities in stratified fluids. *Phys. Rev.* A **31** (1), 410–419.

MIKAELIAN, K.O. 1990 Rayleigh–Taylor and Richtmyer–Meshkov instabilities and mixing in stratified spherical shells. *Phys. Rev.* A **42** (6), 3400–3420.

MIKAELIAN, K.O. 2005 Rayleigh–Taylor and Richtmyer–Meshkov instabilities and mixing in stratified cylindrical shells. *Phys. Fluids* **17** (9), 094105.

OTT, E. 1972 Nonlinear evolution of the Rayleigh–Taylor instability of a thin layer. *Phys. Rev. Lett.* **29** (21), 1429–1432.

PLESSET, M.S. 1954 On the stability of fluid flows with spherical symmetry. *J. Appl. Phys.* **25** (1), 96–98.

RAYLEIGH, LORD 1883 Investigation of the character of the equilibrium of an incompressible heavy fluid of variable density. *Proc. Lond. Math. Soc.* **s1–14** (1), 170–177.

RICHTMYER, R.D. 1960 Taylor instability in shock acceleration of compressible fluids. *Commun. Pure Appl. Maths* **13** (2), 297–319.

SCHWENDEMAN, D.W. & WHITHAM, G.B. 1987 On converging shock waves. *Proc. R. Soc. Lond.* A **413** (1845), 297–311.

SUN, R., DING, J., ZHAI, Z., SI, T. & LUO, X. 2020 Convergent Richtmyer–Meshkov instability of heavy gas layer with perturbed inner surface. *J. Fluid Mech.* **902**, A3.

TAYLOR, G.I. 1950 The instability of liquid surfaces when accelerated in a direction perpendicular to their planes. I. *Proc. R. Soc. Lond.* A **201** (1065), 192–196.

WALCHLI, B. & THORNBER, B. 2017 Reynolds number effects on the single-mode Richtmyer–Meshkov instability. *Phys. Rev.* E **95** (1), 013104.

WEIR, S.T., CHANDLER, E.A. & GOODWIN, B.T. 1998 Rayleigh–Taylor instability experiments examining feedthrough growth in an incompressible, convergent geometry. *Phys. Rev. Lett.* **80** (17), 3763–3766.

WU, J., LIU, H. & XIAO, Z. 2021 Refined modelling of the single-mode cylindrical Richtmyer–Meshkov instability. *J. Fluid Mech.* **908**, A9.

YAN, Z., FU, Y., WANG, L., YU, C. & LI, X. 2022 Effect of chemical reaction on mixing transition and turbulent statistics of cylindrical Richtmyer–Meshkov instability. *J. Fluid Mech.* **941**, A55.

ZHANG, S., LIU, H., KANG, W., XIAO, Z., TAO, J., ZHANG, P., ZHANG, W. & HE, X.-T. 2020 Coupling effects and thin-shell corrections for surface instabilities of cylindrical fluid shells. *Phys. Rev.* E **101** (2), 023108.

ZHAO, Z., WANG, P., LIU, N.-S. & LU, X.-Y. 2020 Analytical model of nonlinear evolution of single-mode Rayleigh–Taylor instability in cylindrical geometry. *J. Fluid Mech.* **900**, A24.

ZHAO, Z., WANG, P., LIU, N.-S. & LU, X.-Y. 2021 Scaling law of mixing layer in cylindrical Rayleigh–Taylor turbulence. *Phys. Rev.* E **104** (5), 055104.

ZHOU, Y. 2017*a* Rayleigh–Taylor and Richtmyer–Meshkov instability induced flow, turbulence, and mixing. I. *Phys. Rep.* **720–722**, 1–136.

ZHOU, Y. 2017*b* Rayleigh–Taylor and Richtmyer–Meshkov instability induced flow, turbulence, and mixing. II. *Phys. Rep.* **723–725**, 1–160.

ZHOU, Y., *et al.* 2021 Rayleigh–Taylor and Richtmyer–Meshkov instabilities: a journey through scales. *Physica* D **423**, 132838.

ZHOU, Y., CLARK, T.T., CLARK, D.S., GAIL GLENDINNING, S., AARON SKINNER, M., HUNTINGTON, C.M., HURRICANE, O.A., DIMITS, A.M. & REMINGTON, B.A. 2019 Turbulent mixing and transition criteria of flows induced by hydrodynamic instabilities. *Phys. Plasmas* **26** (8), 080901.

ZOU, L., AL-MAROUF, M., CHENG, W., SAMTANEY, R., DING, J. & LUO, X. 2019 Richtmyer–Meshkov instability of an unperturbed interface subjected to a diffracted convergent shock. *J. Fluid Mech.* **879**, 448–467.